# Mechanical behaviour and in situ observation of shear bands in ultrafine grained Pd and Pd–Ag alloys

K. Yang [a,*], Yu. Ivanisenko [b], A. Caron [a], A. Chuvilin [c], L. Kurmanaeva [b], T. Scherer [b], R.Z. Valiev [d], H.-J. Fecht [a,b]

[a] *Institut für Mikro- und Nanomaterialien, Universität Ulm, Ulm, Germany*
[b] *Institut für Nanotechnologie, Forschungszentrum Karlsruhe, Karlsruhe, Germany*
[c] *Materialwissenschaftliche Elektronenmikroskopie, Universität Ulm, Ulm, Germany*
[d] *Institute of Physics of Advanced Materials, Ufa State Aviation Technical University, Ufa, Russia*

## Abstract

An in situ tensile test with grey scale correlation has been performed to study the deformation process in ultrafine grained (UFG) Pd and Pd–$x$ at.% Ag ($x = 5$ or 20) alloys produced by high-pressure torsion. Shear band nucleation and propagation was found to be an important deformation mechanism after strain localization during the tensile test. The underlying microscopic mechanism is related to cooperative grain boundary sliding. Moreover, the additional influence of stacking fault energy was found to change the nature of the deformation mechanism from localized strain in Pd to more homogeneous deformation in Pd–20% Ag. In situ analysis and the findings are new and give innovative insight into the basics of deformation in UFG face-centred cubic metals.
© 2009 Acta Materialia Inc. Published by Elsevier Ltd. All rights reserved.

*Keywords:* In situ tensile test; Grey scale correlation analysis; Ultrafine grained materials; High-pressure torsion

## 1. Introduction

Despite the fact that the mechanical behaviour of nanocrystalline (NC) and ultrafine grained (UFG) materials has been studied for decades the basic principles are still not understood [1–7]. For example, despite their superior tensile strength, a very limited uniform elongation due to rapid localization of plastic flow in the neck region is typical of UFG materials, and it greatly restricts their practical application. The primary reason for such behaviour is related to the limited strain hardening capacity due to the difficulty in storing dislocations in very small grains.

In the recent past several approaches have been suggested to improve the strain hardening capacity of fine grained materials, for example a high density of twin boundaries in the interior of nanograins, producing a bi-modal grain size distribution or producing a uniformly distributed array of fine precipitates [8]. Here an attempt is made to (i) investigate the basic principles of plastic deformation of UFG Pd and Pd–Ag alloys by in situ SEM analysis and (ii) enhance their strain hardening capacity by modifying the stacking fault energy of UFG Pd–Ag alloys in solid solution in a controlled manner [9].

As mentioned above, usually UFG and NC metals and alloys have a propensity for strain localization [10–13], which often sets in immediately after the yield point. In a systematic study of compression tests of bcc Fe [14] shear localization with intense strain accumulating in the narrow shear bands was seen to occur immediately after the onset of plastic deformation for all specimens with smaller grain sizes ($d < 300$ nm) at both high and low strain rates. Fully dense NC Cu produced by an in situ consolidation technique was also reported to be susceptible to shear localiza-

---

[*] Corresponding author. Address: Universitat Ulm, Institut fur Mikro- und Nanomaterialien, Albert-Einstein-Allee 47, D-89081 Ulm, Germany. Tel.: +49 731 50 25408.

*E-mail address:* kejing.yang@uni-ulm.de (K. Yang).

tion during tensile tests at low strain rate [15]. In abundant reports on mechanical testing of other UFG and NC materials [16–20] shear localization appears to be the basic failure mechanism, which is mainly mediated by grain size, although its particular features, such as shear band morphology, etc., varied depending on the specific sample (microstructure, preparation routine) and testing conditions. For example, the morphology of shear bands in bcc Fe [14] showed well-defined boundaries with band widths of several micrometres, whereas the shear markings of face-centred cubic (fcc) metals are narrow and difficult to resolve [21–23]. Conjugated shear bands are observed in body-centred cubic (bcc) Fe [14], while fcc metals showed single oriented sets of shear bands [15]. Several groups have attributed shear propensity in UFG and NC materials to increased strength and decreased strain hardening capabilities. However, the underlying mechanism of shear band formation still needs further exploration.

Due to rapid strain localization and the complex geometry of the neck, it is challenging to determine the actual flow stress after strain localization in tensile tests, which hinder strain hardening analysis of UFG materials. Several models were suggested to predict the shape of the forming neck using finite element modeling [24], but all of them are only applicable to cylindrical specimens. Here we demonstrate for the first time direct visualization of the necking process by in situ observation combined with grey scale analysis. This has allowed us to find out not only the necessary parameters for strain hardening analysis in the post-necking range, but also to reveal macroscopic and mesoscopic processes, such as shear banding, fracture and accompanying deformation, in UFG Pd and Pd–$x$ at.% Ag ($x = 5$ or 20) alloys produced by high-pressure torsion (HPT) [10] in a dedicated scanning electron microscope. The addition of Ag decreases the stacking fault energy of Pd from 190 to 175 mJ m$^{-2}$ in Pd–5% Ag and 125 mJ m$^{-2}$ in Pd–20% Ag [25]. It can be expected that modification of the stacking fault energy has an influence not only on strain hardening but also on the general deformation mechanism and fracture.

## 2. Experimental procedures

Pd and Pd–$x$ at.% Ag ($x = 5$ or 20) alloys were melted in an arc melting oven under an Ar atmosphere. Appropriate samples were cut into discs 10 mm in diameter and 0.3 mm in thickness and processed by HPT under a quasi-hydrostatic pressure of 6 GPa for five rotations [10]. Samples for transmission electron microscopy (TEM) were prepared by electropolishing with a BK-2 electrolyte [26] at −20 °C at a voltage of 60 V using a Tenupol 5 electropolishing apparatus (Struers A/S). TEM specimens were taken from a location corresponding to the gauge section of the tensile specimen parallel to the shear plane of HPT (plane XOY in Fig. 1a). For post-testing investigation, specimens were extracted from the neck area of tensile specimens by the focused ion beam technique using an FEI Strata 400. From these, thin

TEM specimens were cut out parallel to the fracture surface (ZOY) as shown in Fig. 1b. For conventional bright and dark field imaging Philips CM 30 and Titan 80–300 electron microscopes, both operated at 300 kV, were used. The mean grain size was estimated using a line interception method [27] in at least five randomly selected typical dark field TEM images, each containing at least 60 grains under the Bragg condition. The line intercepts were measured in two directions: in the direction of shear deformation during HPT, and perpendicular to it. The final grain size was calculated as the average of length and width.

For miniature tensile tests the HPT samples were cut into a "dog-bone shape" with a gauge length of ∼1.2 mm and width of ∼1 mm. Careful polishing was carried out to remove surface defects as potential stress concentration sites. Specimens with a final thickness of ∼0.3 mm were fixed in a MicroDAC (Kammrath and Weiss GmbH) tensile test stage and were installed in a LEO 1550 high-resolution field-emission scanning electron microscope (FE-SEM). The in situ tensile testing was typically carried out with a constant strain rate of 10$^{-3}$ s$^{-1}$. The stress–strain curve was recorded during the deformation process and a sequence of micrographs was taken during loading. Elongation in the gauge length was corrected by performing grey scale correlation analysis of the recorded micrographs. This digital image processing method determines the local displacement of pre-defined points in the reference image by correlating the grey scale matrices of both the reference and comparative images and tracing their maximum correlation factor [28]. In the present study the two-dimensional pre-defined square network of points (40 × 28) was applied to the gauge length, which occupied 1024 × 630 pixels. A small submatrix (30 × 30 pixels) was taken from the area surrounding a desired measuring point in the reference image. A search was then made for the most similar submatrix within a field (50 × 50 pixels) around the corresponding point in the comparative image. Similarity between the submatrices in the reference and comparative images was identified from the highest cross-correlation factor, which was determined by applying two-dimensional cross-correlation analysis to local grey scale values. By performing grey scale correlation for the whole network of points the displacement map could be determined. It is worth mentioning that grey scale correlation can only present two-dimensional material flow on the sample surface (which describes the plane stress straining well) but cannot fully represent the complex three-dimensional strain state which forms after the onset of necking. However, it does offer valuable information on the mesoscopic deformation process.

The fracture surfaces were studied in the aforementioned scanning electron microscope. Atomic force microscopy (AFM) images were recorded using the contact and tapping modes [29,30] using an ultraobjective manufactured by Fries Research Technology and a Digital Instruments DI 3000. The topography of the shear bands situated on the specimen surface was quantitatively characterized in contact mode with an applied force of 1.7 μN.
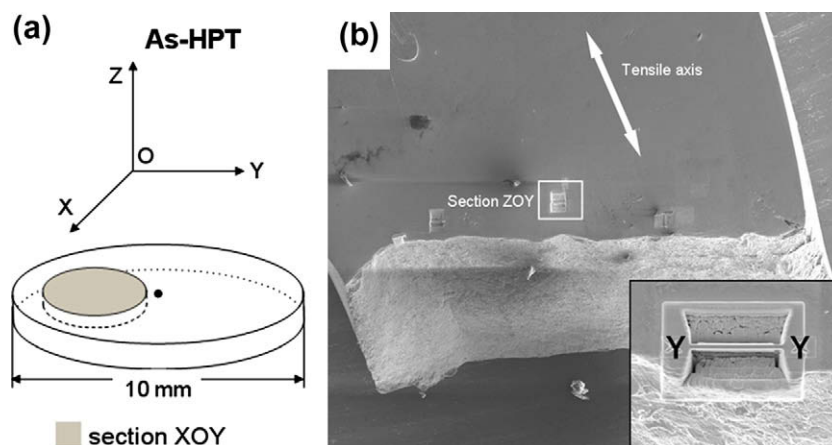
Fig. 1. (a) Schematic diagram of sample cutting from an as HPT disc for TEM investigation. The grey circle indicates the position of the TEM thin foil. (b) FIB cutting for post- deformation TEM investigation of the microstructure in the neck. An enlarged image of the thin lamella in section ZOY, in close vicinity to fracture surface.

Additionally, features on the fracture surface were captured from the phase contrast in AFM tapping mode at the first free bending resonance frequency of the cantilever, i.e. 158–168 kHz for stiff diamond-coated Si cantilevers. The advantage of phase imaging as compared with topography imaging in AFM is that in the first case the image contrast changes according to the short wavelength topography, whereas this is often overshadowed by the long wavelength topography in topography images, hence phase imaging reveals finer detail. Generally, the phase image depicts the phase shift between cantilever vibration and the excitation signal, which reflects the non-elastic impact between tip and sample surface [31,32]. With decreasing topography wavelength the characteristic dimension of the surface becomes comparable with the contact radius between the tip and surface. In this case slight changes in the contact area, due to grain boundaries for example, result in magnitude changes in the dissipated energy during impact, thus leading to a change in the cantilever vibration phase angle.

## 3. Results

### 3.1. Microstructure characterization

Typical TEM dark field images of as prepared HPT Pd and Pd–Ag alloys are shown in Fig. 2a,c and e. The microstructure of all samples was characterized by slightly elongated grains with an aspect ratio of ∼1.5. The mean grain size of as HPT Pd and Pd–5% Ag was ∼240 nm. Grains were delineated by narrow and distinct grain boundaries; in some grains dislocation subboundaries could be seen. The dislocation density in Pd was rather low, i.e. only a few dislocations were present in each grain, and the number of dislocations next to grain boundaries was higher than that in central parts (Fig. 2b). In Pd–5% Ag the dislocation density was notably increased (Fig. 2d). Alloyed samples exhibited a decrease in grain size as compared with unalloyed samples prepared under the same conditions. For, example Pd–20% Ag had a mean grain size of ∼150 nm and the dislocation density was notably higher than that in pure Pd, as dislocation tangles and pile-ups could be found in the majority of grains (Fig. 2f). Furthermore, atomic resolution TEM investigations revealed numerous stacking faults (SFs) and stacking fault tetrahedra (SFTs) laying in the (1 1 1) planes, as shown in Fig. 3. Grain boundaries resulting from severe plastic deformation (SPD) were in a non-equilibrium state; they contained a large number of extrinsic grain boundary dislocations and represented the source of long-range internal stresses [10]. Typical examples of non-equilibrium grain boundaries in the microstructure of HPT processed Pd and Pd–Ag alloys are shown in Fig. 4a and b.

Additionally, the microstructure of Pd–20% Ag in the neck area was investigated after tensile test. At low magnification small pores with diameters of 30–50 nm were observed by TEM (not shown here); these pores were formed as a result of nanovoid formation and growth during tensile straining and represent the nuclei of dimples found on the fracture surface [33]. In cross-sections taken parallel to the fracture surface (Fig. 5a) grains elongated parallel to fracture surface, i.e. along the shear direction, can be clearly seen. The grain length along the long axis increased from 185 nm in the as HPT state to 222 nm. Some indications of alignment of neighbouring grain boundary segments in parallel can be seen in Fig. 5a. Moreover, high-resolution TEM reveals plentiful SFs and SFTs of ∼3 nm. Fig. 5b shows at least three SFs and six SFTs in an area of $35 \times 35$ nm$^2$, which corresponds to a density of partial dislocations of $\sim 2.2 \times 10^{16}$ m$^{-2}$.

### 3.2. Mechanical behaviour

Tensile tests were performed in situ with a testing apparatus specifically designed and constructed for the small specimens under investigations. In order to elucidate the
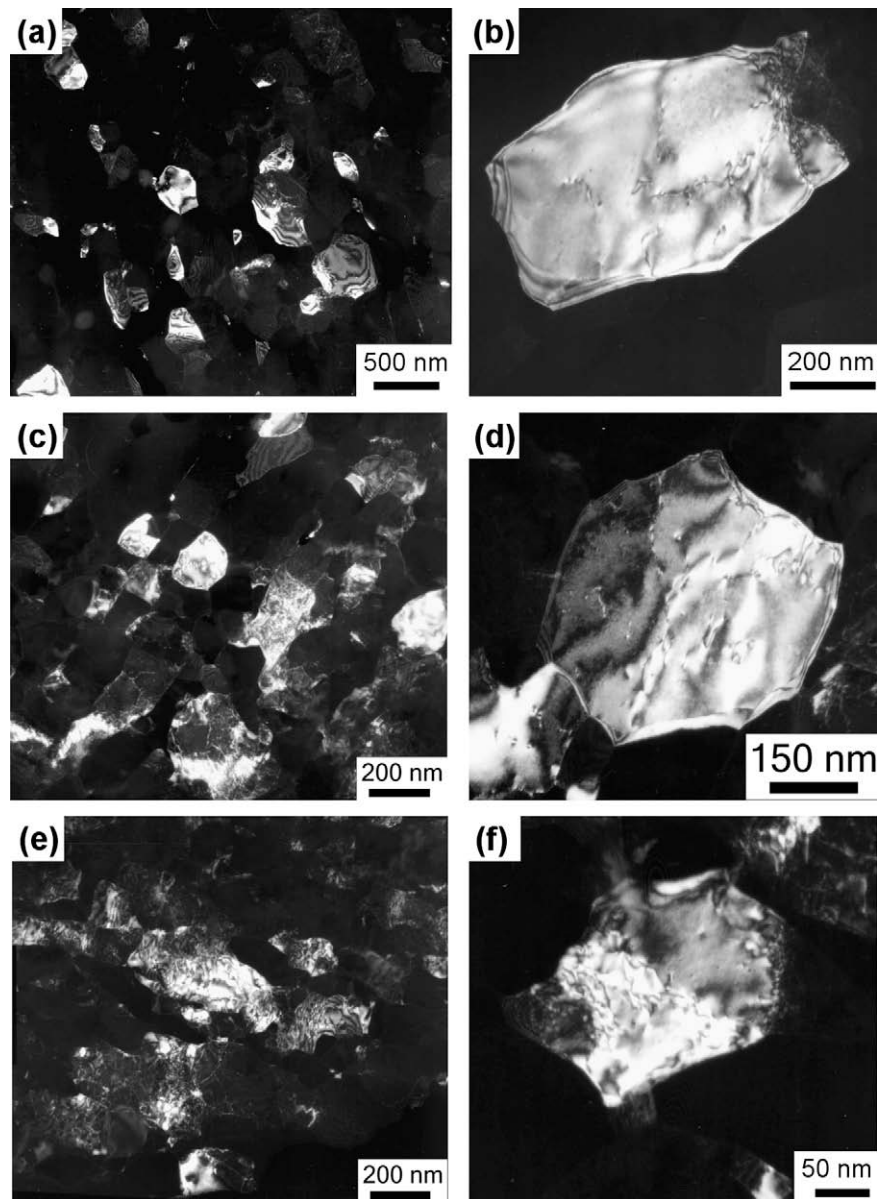
Fig. 2. Dark field TEM micrographs showing the microstructure of as HPT (a and b) Pd, (c and d) Pd–5% Ag and (e and f) Pd–20% Ag alloys.

intrinsic mechanical response of the samples, the engineering stress ($\sigma_e$)–engineering strain ($\varepsilon_e$) curves (Fig. 6a, solid lines) were converted to true stress ($\sigma_t$)–true strain ($\varepsilon_t$) curves (Fig. 6a, dashed lines) using the equations:

$$\sigma_t = \sigma_e(1 + \varepsilon_e), \quad \varepsilon_t = \ln(1 + \varepsilon_e) \tag{1}$$

After the onset of necking Eq. (1) cannot be used, because the formation of a neck introduces a complex tri-axial state of stress in that region. The necked region is in effect a mild notch. A notch under tension produces radial stress and transverse stress, which increase the value of longitudinal stress required to cause plastic flow. As a realistic and relatively simple estimate the average true stress in the neck was determined by dividing the axial tensile load by the minimum cross-sectional area of the specimen at the neck. For that, the cross-sectional width of the

specimen was taken from micrographs obtained in situ and the thickness was interpolated from that at the onset of strain localization and that at fracture, assuming a rectangular geometry.

From Fig. 6a it is obvious that the onset of strain localization was delayed with increasing Ag concentration; the uniform plastic strain increased by a factor of ~2 from 0.028 for Pd to 0.050 for Pd–20% Ag alloy. Furthermore, alloying led to a notable increase in the strength of HPT Pd; both yield stress (YS) and ultimate tensile strength (UTS) increased almost linearly from 500 (YS) and 660 MPa (UTS) for Pd to 950 (YS) and 1230 MPa (UTS) for Pd–20% Ag (Table 1).

The normalized strain hardening rate $\Theta$, which is defined by $\Theta = 1/\sigma(\delta\sigma/\delta\varepsilon)$ is represented for all the alloys studied in Fig. 6b. It is apparent that $\Theta$ is notably greater
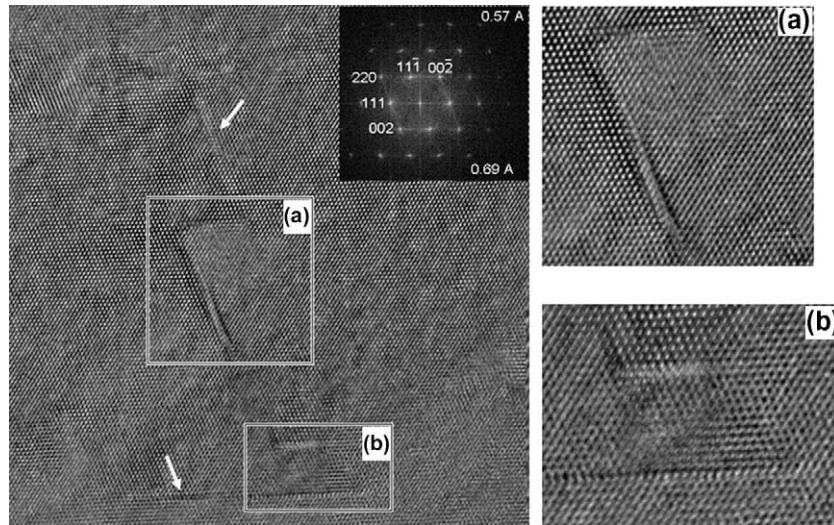
Fig. 3. HRTEM image of stacking faults in as HPT Pd–20% Ag viewed along ⟨1 1 0⟩. Corresponding FFT. Several SFs are indicated by arrows and two stacking fault tetrahedrons are shown enlarged in (a) and (b).
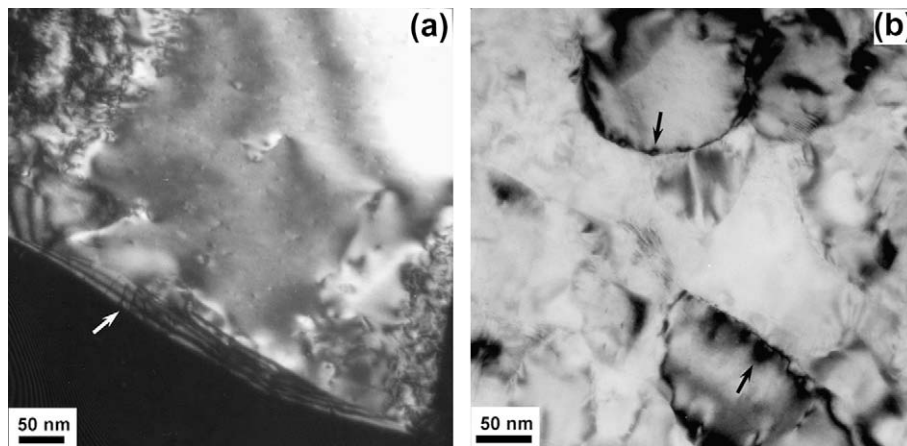


Fig. 4. Examples of non-equilibrium grain boundaries in HPT processed Pd and Pd–Ag alloys. (a) Dark field image of pure Pd showing lattice dislocations entering the grain boundary as shown by the arrow. (b) Bright field image of the Pd–20% Ag alloy showing bow-like diffraction contrast at the grain boundaries, indicating high internal stresses at GB.
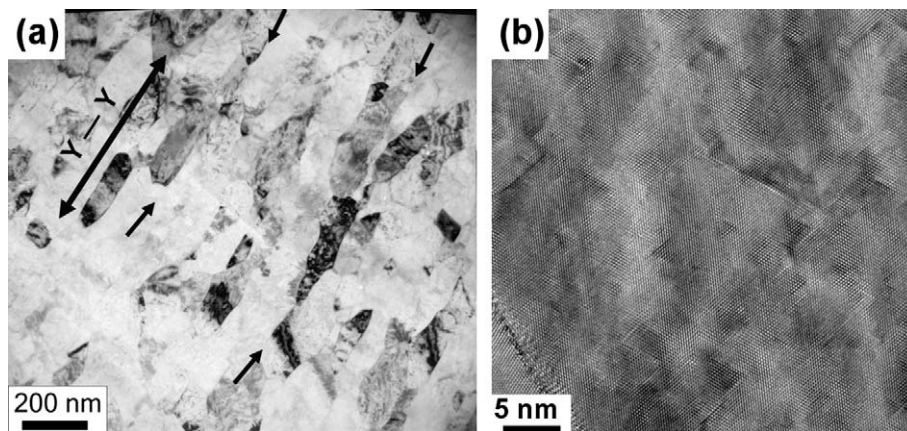


Fig. 5. Post-deformation characterization of Pd–20% Ag in the neck area. (a) Bright field image of section ZOY. The double arrow Y–Y indicates the orientation of the specimen (see insert to Fig. 1b). Arrows indicate the alignment of neighbouring grain boundary segments in parallel. (b) HRTEM image viewed along ⟨110⟩ showing plentiful SFs and SFTs.
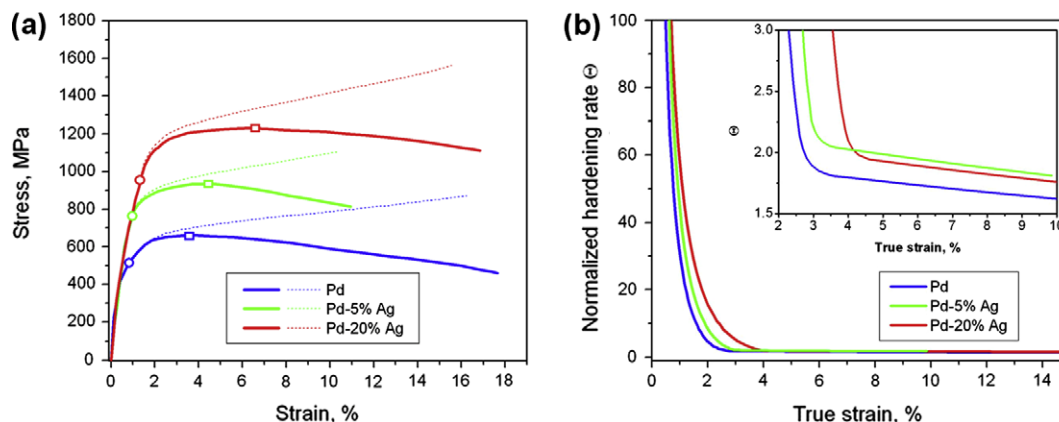
Fig. 6. (a) Tensile engineering (solid lines) and true stress–true strain curves (dashed lines) of UFG Pd, Pd–5% Ag and Pd–20% Ag. The circles indicate yielding and the squares the UTS. (b) The normalized strain hardening rate against true strain. Insert shows $\Theta$ after necking.

Table 1
Stacking fault energy ($\gamma_{SF}$), mean grain size and main mechanical parameters of pure Pd and Pd–$x$ at.% Ag ($x = 5$ or 20) alloys.

|  | Pd | Pd–5% Ag | Pd–20% Ag |
|---|---|---|---|
| $\gamma_{SF}$ (mJ m$^{-2}$) | 190 | 175 | 125 |
| Mean grain size (nm) | 240 | 240 | 150 |
| YS (MPa) | 500 | 750 | 950 |
| UTS (MPa) | 660 | 935 | 1230 |
| Uniform elongation | 0.028 | 0.035 | 0.050 |

for Pd–20% Ag in the uniform strain range. On the other hand, after onset of strain localization a saturation of hardening was observed, however, $\Theta$ remained slightly higher in the alloys as compared with pure Pd (see insert in Fig. 6b).

### 3.3. The deformation process revealed by in situ tests and grey scale correlation

The in situ tensile testing of Pd and Pd–Ag alloys revealed a deformation process which can be basically represented by three stages: uniform elastic and plastic deformation, localized flow in the neck region and crack initiation/propagation. At the beginning of loading the specimen was stretched homogeneously throughout the entire gauge length, with an axis-symmetrical stress–strain state. When the UTS was reached instability was triggered by stress concentration sites, e.g. inhomogeneities in defect distribution, causing deformation to become localized and consequently macroscopic necking commenced. Fig. 7 shows a grey scale analysis of the plastic flow in the gauge length in Pd and Pd–Ag alloys after the onset of necking at a true strain of 0.1. Inspection of the displacement contour of Pd revealed a distinct X-shaped region within which material flowed primarily transversely. This resulted in two wedge-shaped regions sinking inwards progressively (Fig. 7d); meanwhile, material flowed across the boundary of the X-region to accommodate the tensile strain (Fig. 7a).

However, the grey scale analysis can display the plastic flow in only two dimensions: in the tensile and transverse directions. In reality a tri-axial strain state develops in

the neck area (analogous to the tri-axial stress state), i.e. the specimen thickness (normal direction) is reduced at the same time, as revealed by investigation of the fracture surface. Thus the tensile strain is mainly accommodated within the neck region, by contraction in both the transverse and normal directions. In the Pd sample, at a certain strain strain localization became restricted within a material layer inclined around 50° to the tensile axis. Extended shear along this layer led to shear fracture. A crack was generated in the centre of the X-region, where thinning was severe. Similar developments, but with less pronounced necking and shearing, occurred in Pd–5% Ag (Fig. 7b and e). However, in contrast to the obvious X-region in Pd and Pd–5% Ag, Pd–20% Ag showed relatively homogeneous elongation before and even after the onset of strain localization. As can be noted in Fig. 7c and f the strain was dispersed throughout the gauge length in the tensile as well as in the transverse directions, only a narrow and shallow X-region formed. The fracture surface of Pd–20% Ag barely exhibited shearing but showed relatively homogeneous thinning (not confined within the necking region). The above observations indicate that resistance to localized deformation was greatly improved while neck formation was retarded by the addition of 20% Ag.

### 3.4. Deformation relief

The advantage of in situ tests is that they can directly visualize the mesoscopic evolution of the deformation process. Similar developments in surface relief are observed in all samples before fracture. As exemplified by Pd–20% Ag, after the onset of strain localization the neck region manifests obvious surface roughening when comparing the topographies of the same site at the beginning and mid way through the tensile test (Fig. 8a and inset). Within the neck the surface is uniformly covered with microscopic shear bands oriented ~50° to the loading axis, as shown in Fig. 8a. The morphologies of the micro SBs in Pd and the Pd–Ag alloys demonstrated a tendency for decreasing SBs spacing and height with increasing Ag concentration.
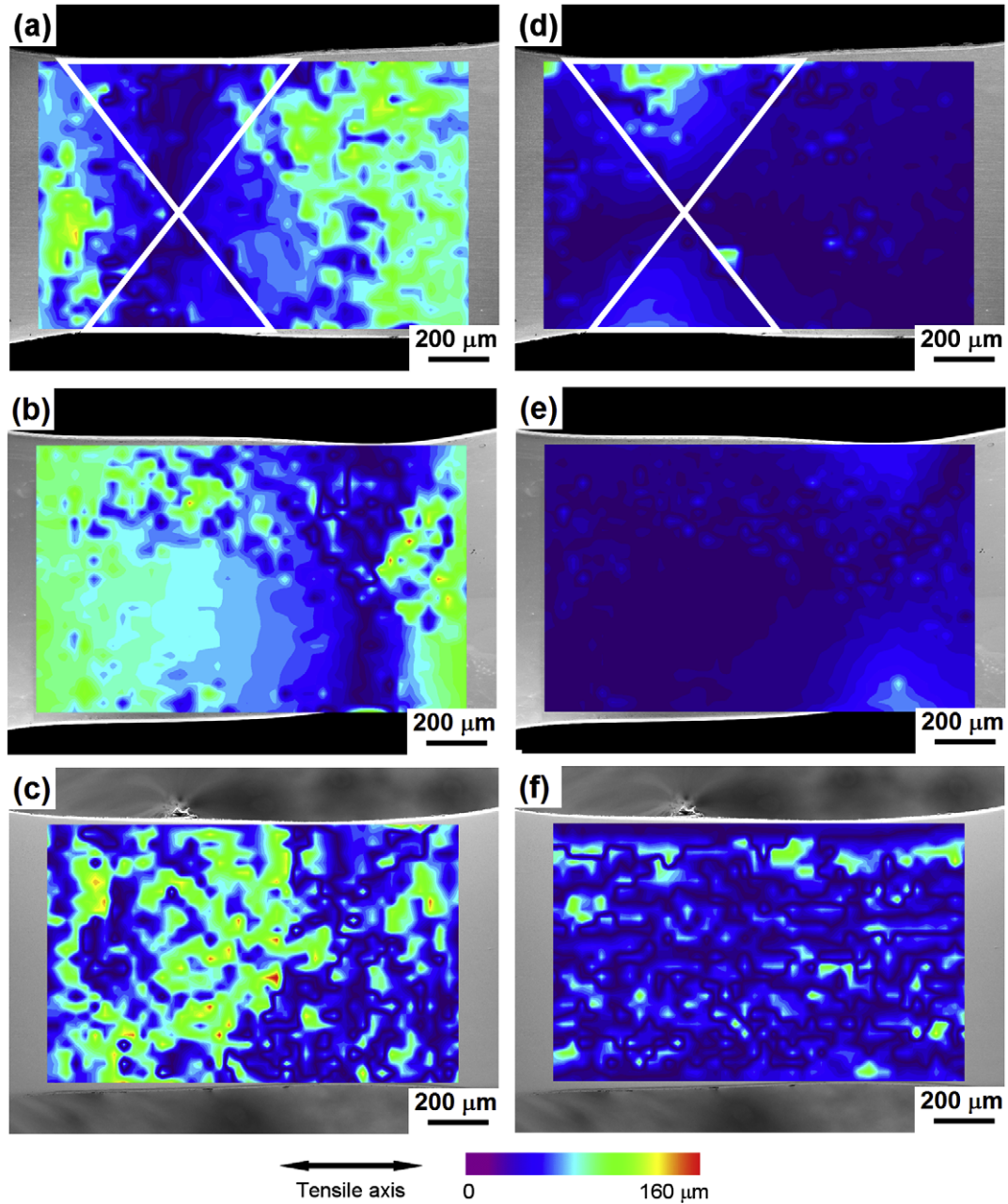
Fig. 7. Grey scale correlation analysis of plastic deformation in (a and d) Pd, (b and e) Pd–5% Ag and (c and f) Pd–20% Ag at a strain of 0.1. (a–c) Displacement of pre-defined points showing material flow in the tensile direction and (d–f) in the transverse direction. The displacements are illustrated by the color contour, whose magnitude is defined by the color bar. Note that the displacement does not simply correspond to the local displacement at each point but the accumulated displacement of points along the horizontal/perpendicular lines. The X-regions are shown in (a and d).

The micro SBs in Pd and Pd–20% Ag were investigated after deformation by AFM (Fig. 9). Considering that both samples ruptured at similar strains to failure it is worth comparing the parameters of the micro SBs. According to the height profiles, drawn perpendicular to the SB direction (Fig. 9a and b), these micro SBs were mainly ditch-like. The micro SBs in Pd–20% Ag were characterized by finer spacing (~1 μm) and a smaller ditch height (~10–35 nm), while Pd had wider spacing (~2–5 μm) and a more pronounced height (~10–70 nm) (Table 2).

### 3.5. Fracture

Another interesting observation was the distinct difference in fracture processes occurring in Pd and Pd–20% Ag. In Pd the crack initialized in the mid plane of the specimen with a large increase in the multiplication of shear bands (Fig. 8c). The path of crack propagation coincided with the direction of former micro SBs. Extension of the crack by severe shearing led to a typical shear fracture. However, the fracture in the Pd–20% Ag specimen developed quite
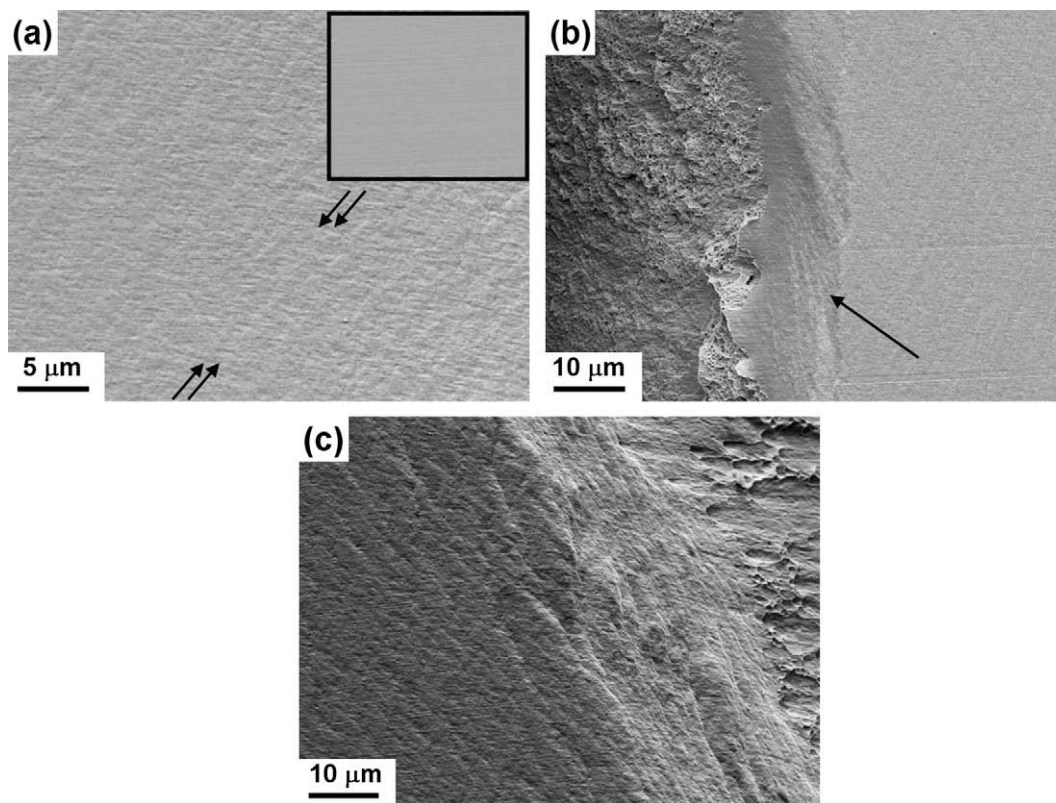
Fig. 8. (a and b) Deformation relief development at the beginning of straining, during straining and after fracture in Pd–20% Ag. (a) Micro shear bands indicated by the black arrows are orientated ~50° to the loading axis within the X-region. The corresponding area before necking at the same magnification is shown in the insert. (b) Newly formed bundle of shear bands in the vicinity of the fracture surface. (c) Deformation relief at the fracture edge in Pd.

rapidly, without extended shearing. New bundles of SBs with a different orientation to the earlier micro SBs were generated immediately before fracture (Fig. 8b). The AFM topography of the sample surface in the vicinity of the fracture edge revealed ditch-like as well as step-like SBs in both Pd and Pd–20% Ag (Fig. 9c and d). These SBs in Pd had the same orientation as the micro SBs, but a more pronounced shear height (~20–150 nm) (Table 2). It is plausible that they originated by the development of earlier micro SBs. Nevertheless, the shear bands leading to the final rupture of Pd–20% Ag exhibited a larger shear height (~10–70 nm) (Table 2) as compared with that of the micro SBs and a quite different orientation, at 80° to the tensile axis (Fig. 8b).

The fracture surface of all specimens was characterized by a dimple structure. In addition to dimples, which are typical of ductile fracture, new macroscopic features were revealed on the fracture surfaces of all studied specimens. In Fig. 10a characteristic linear features parallel to the tensile specimen plane (which coincides with the HPT shear plane) can be seen. We conclude that the lines represent shear bands formed during previous HPT deformation. Sometimes these SBs were opened and sheared during the tensile test, as shown in Fig. 10b. AFM phase images of the as formed free surface (Fig. 10c) revealed rough convex structures with pronounced grooves passing between hummock-like features with a size of ~0.1–0.3 μm. We assume that these hummock-like features represent grains and

grain clusters. Formation of shear bands by the alignment of grains with collinear grain boundaries could be clearly identified.

## 4. Discussion

The present study has demonstrated that alloying leads not only to an increase in the yield stress and ultimate tensile stress in Pd–20% Ag, but also to a notable improvement in the uniform elongation and the strain hardening rate compared with pure Pd. Whereas enhancement of the yield stress in the Pd–20% Ag alloy was mostly related to the smaller grain size and higher dislocation density as compared with those in Pd and the Pd–5% Ag alloy, the increase in UTS and uniform elongation was most probably associated with an improved strain hardening ability. Solid solution hardening can clearly be excluded as a dominant factor since the effect was small in the range 20 MPa, i.e. about 1.5% [34]. The present investigation focused on the post-necking regime. Although all studied samples demonstrated strain localization (necking), necking was more pronounced in pure Pd and Pd–5% Ag and less developed in Pd–20% Ag.

Analysis of the strain hardening behaviour (Fig. 6b) revealed two strain hardening rate change regimes in the studied range of strains, presumably pointing to the domination of two different mechanisms of plastic deformation.
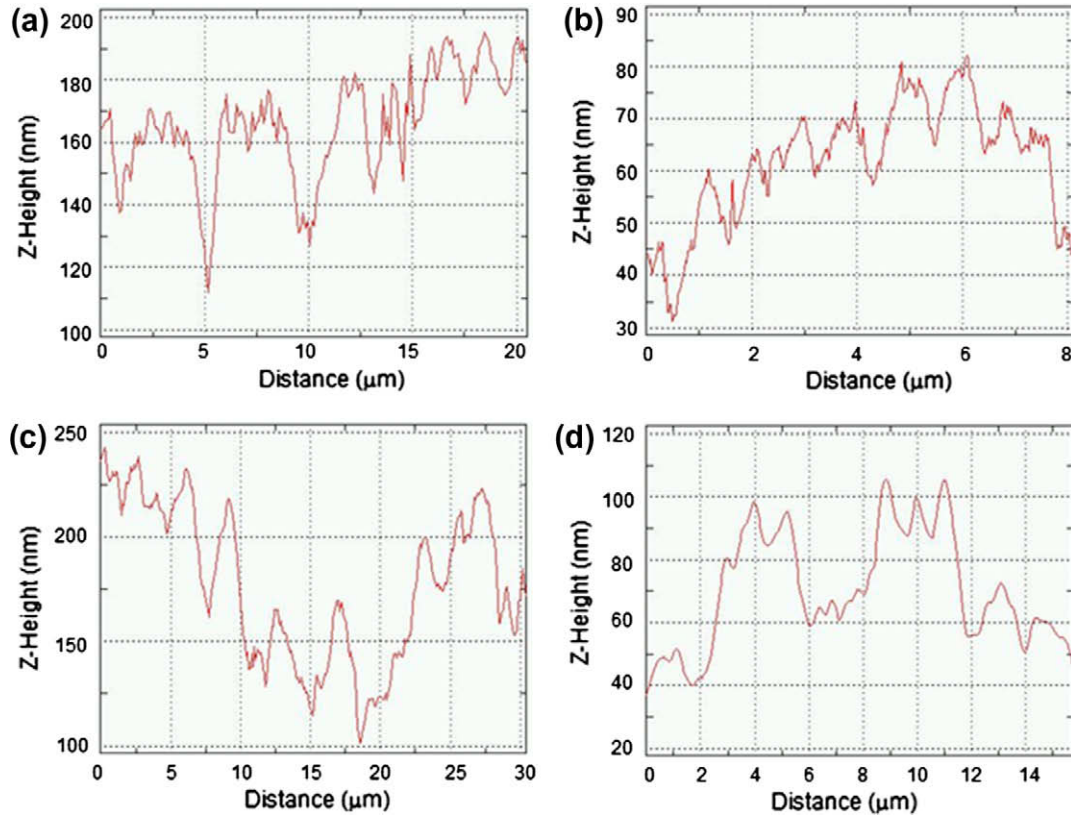
Fig. 9. AFM linear height profiles showing different morphologies of shear bands. (a and b) Ditch-like micro shear bands away from the fracture edges. (c and d) Step-like shear bands in the vicinity of the fracture edges. (a and c) Pd and (b and d) Pd–20% Ag.

Table 2
Shear bands parameters of micro shear bands (a) away from the fracture edge and (b) in close vicinity to the fracture edge in Pd and Pd–20% Ag.

| Shear band | Pd | Pd–20% Ag |
|---|---|---|
| a | Spacing ~2–5 μm<br>Height ~10–70 nm | Spacing ~1 μm<br>Height ~10–35 nm |
| b | Spacing ~2–8 μm<br>Height ~20–150 nm | Spacing ~1–4 μm<br>Height ~10–70 nm |

In the first regime, corresponding to uniform strain, $\Theta$ gradually decreases and remains clearly higher for the Pd–20% Ag alloy. In this range of strains deformation is mediated by dislocation slip and the strain hardening rate is determined by the ability of the material to store dislocations. This ability is higher in the Pd–20% Ag alloy due to its lower stacking fault energy. After the onset of necking this deformation stage is terminated, as shown by an abrupt change in the strain hardening rate curve in Fig. 6b. In order to understand the reasons for such a drastic change in strain hardening behaviour we need to analyse the microstructure features that developed in the neck area. These features were revealed to exist on three levels. On macroscopic level we observed the appearance and development of shear bands, on the mesoscopic level the formation of planes of cooperative grain boundary sliding and on the microscopic level signatures of dislocation slip in the

form of grain shape changes. These features will be addressed in the following sections.

### 4.1. Shear banding and cooperative grain boundary sliding

Careful inspection of the neck surface revealed that its formation was accompanied by the appearance of shear bands. In coarse crystalline materials deformed at high strains and strain rates shear bands represent narrow areas of intense shear that occur "independently of the grain structure and of normal crystallographic considerations", but are generally restricted to one or at the most a few contiguous grains [35]. Thus, strain localization may be due to geometrical or thermal softening [36,37]. UFG materials, however, often deform via shear banding at rather low strains and strain rates and shear bands expand over many grains [38,39]. Those shear bands in UFG materials whose width/grain size ratio falls in the range 1–10 are categorized as micro shear bands [39].

The non-crystallographic nature of shear bands seems to suggest that its theoretical description must be mainly based on continuum mechanics, irrespective of a crystal or amorphous structure [40]. However, discrepancies between the macroscopic features of shear bands in bulk metallic glasses (BMG) and in UFG metals reveal that shear band formation, and consequently its role in plastic deformation, is closely connected to specific microstruc-
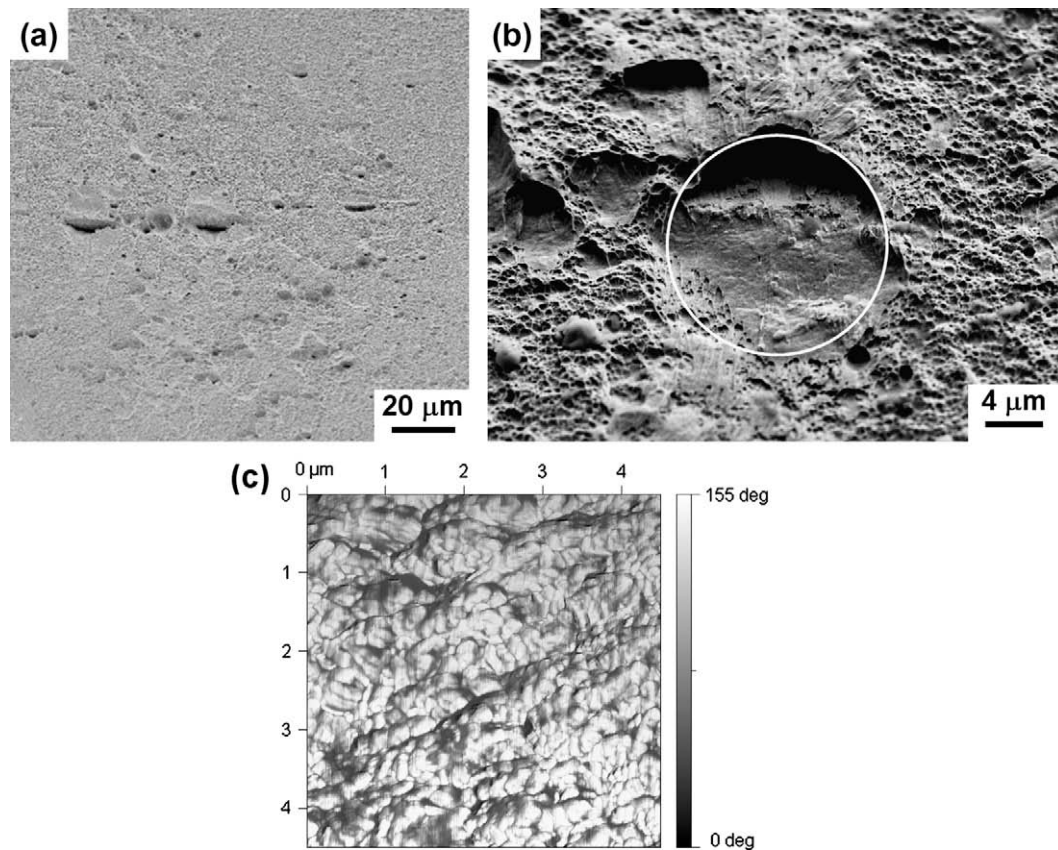
Fig. 10. Fracture surface in Pd–20% Ag alloy. (a) SEM overview image showing linear shear bands parallel to the tensile specimen plane. (b) A detailed image showing opened and sheared shear bands (SEM). (c) Phase image taken by tapping mode AFM at the fracture surface indicated by the circle in (b).

tures. In the absence of dislocation and crystallographic slip plastic flow in BMG at a relatively low homologous temperature is accomplished by propagation of shear bands, which are of 10–20 nm thick and with shear steps on the surface up to several micrometres high [41]. A simple estimation of plastic strain carried by a single shear band in BMG indicates apparent heterogeneous deformation. A shear band with a step of 5 μm at approximately 45° to the load axis can reach ∼0.1% of the total strain for a sample of 4 mm length, which is a considerable proportion of the sustainable strain for BMG (normally less than 2%).

In contrast, well-defined thin shear bands are rarely observed in UFG materials. Rather, wavy and profuse micro shear bands are typical. Unlike concentrated shearing within certain bands in BMG, Sabirov et al. found that the activation of micro shear banding could defuse and stabilize against catastrophic macro shearing culminating in failure [39]. In this sense, micro shear bands are capable of carrying plastic strain in a relatively homogeneous manner.

In agreement with a previous report on the deformation behaviour of a UFG Al alloy in tensile tests at a very low strain rate ($10^{-4} \, s^{-1}$) [39], two different SB types were found in the present investigation: ditch-like SBs, which result from micro shearing in the direction of maximum shear stress (Fig. 9a and b), and step-like ones (Fig. 9c

and d). Step-like SBs form mainly just before fracture and obviously play a role as precursors. Ditch-like SBs start to form immediately after the onset of necking and contribute to plastic deformation. Sabirov et al. [39], discussing the deformation mechanisms in a UFG Al alloy, emphasised the significant contribution of shear banding and grain boundary sliding in deformation and argued that the formation of ditch-like micro shear bands is related to grain boundary sliding events. Many reports exploring the microscopic mechanisms responsible for plastic deformation in nanomaterials point to the formation of local shear planes associated with cooperative grain boundary sliding [42–45]. Our TEM observations revealed such cooperative shear planes in the microstructure in the neck area (Fig. 5a). Extension of the mesoscopic shear planes over 20–50 grains may result in the formation of macroscopic shear bands, which is consistent with our observation of intergranular passage (formation) of ditch-like shear bands in Fig. 10c. Note also the very rough appearance of the specimen surface; such an appearance can result from the shuffling and rotation of grains and grain conglomerates upon formation of SBs. It should be emphasised that grain boundaries resulting from SPD are in a non-equilibrium state; they contain a large number of extrinsic grain boundary dislocations and represent the sources of long-range internal stresses [10]. It has frequently been shown that grain boundary sliding is enhanced along non-equilibrium

grain boundaries [46,47], therefore intergranular formation of shear bands resulting from cooperative grain boundary sliding is facilitated in SPD processed materials.

As mentioned before, the majority of SBs observed away from the immediate vicinity of the fracture area were ditch-like micro SBs. Therefore, we conclude that this type of SB is more important in post-necking deformation, while step-like SBs mostly contribute to fracture. In the Pd–20% Ag alloy the frequency of ditch-like SB formation was higher than that in pure Pd (Fig. 9a and b, Table 2), which promotes a more homogeneous distribution of shear and consequently better resistance to strain localization in this alloy. The height of micro SBs was greater in pure Pd, nevertheless it was lower than the mean grain size in all specimens studied (Table 2). The revealed difference in micro SB morphology was more likely related to the smaller grain size in Pd–20% Ag, because intergranular SB formation should be easier in a material with a smaller grain size.

In Fig. 10a the characteristic linear features are suggested to represent SBs formed during previous HPT deformation. It is worth noting that these SBs formed during HPT and the SBs formed during tensile straining were of two different sets. The stress–strain conditions required for these two sets of SBs are quite different: the shear plane emerging during HPT is parallel to the specimen surface, whereas in tensile straining the maximum shear stress acts in the plane perpendicular to the specimen surface but orientated ∼45° to the tensile axis, assuming an ideal case. These two types of SBs lie in different planes. Thus the SBs formed during HPT are unlikely to influence the formation of micro SBs during subsequent tensile tests. However, we cannot exclude the continued growth of SBs formed during HPT during tensile testing if the local stress–strain conditions allow it.

### 4.2. Dislocation slip

Dislocation slip obviously contributes significantly to plastic deformation in the post-necking regime. In the Pd–20% Ag alloy there was a pronounced increase in grain length along its long axis, from 185 to 222 nm, which corresponds to approximately 20% strain due solely to dislocation slip. This value seems to be even larger than the total tensile strain (Fig. 6a), however, one should note that this total strain does not correspond to the actual strain experienced by the specimen. After the onset of necking strain is restricted to an area much shorter than the gauge length, therefore standard equations for the estimation of strain are no longer applicable [48].

Estimation of SF density from Fig. 5b reveals a rather high density of partial dislocations, $\sim 2.2 \times 10^{16}\,\mathrm{m}^{-2}$, which nearly an order magnitude higher than the dislocation density before the tensile test. It is in good agreement with the high strain hardening capacity of Pd–20% Ag alloy during plastic deformation. Moreover, SFTs consisting of intrinsic stacking faults on four {1 1 1} planes locked by six stair-rod dislocations are sessile and may act as a relatively hard obstacle for dislocation motion, as reported in a molecular dynamics simulation [49]. Thus, the high incidence of SFs and SFTs found in Pd–20% Ag may effectively retard the development of a neck after formation. Necking results from multiple slipping when dislocation gliding develops in all possible slip systems. SFs and SFTs, however, may serve as plane barriers to a moving dislocation, leading to the domination of slipping in a single slip system and the suppression of slipping in all other slip systems, resulting in a shallow neck region [50].

## 5. Conclusions

In summary, in situ tensile testing with grey scale correlation is a powerful tool to study the deformation process in miniature specimens. It can uncover almost imperceptible mesoscopic deformation flow and reveal the details of the evolution of surface deformation, which is the footprint of underlying mechanisms. The present study confirms the following.

i. Shear band formation and propagation is a very important mechanism in the plastic deformation of fcc UFG materials, such as UFG Pd and Pd–Ag alloys.
ii. The responsible microscopic mechanism for micro shear banding is related to cooperative grain boundary sliding.
iii. Variation of the stacking fault energy may provide an additional strategy for dislocation storage in UFG materials, leading not only to enhanced strain hardening capacity, but also to better resistance to strain localization after neck formation. First, lowering of the stacking fault energy promotes the formation of grains of smaller size during HPT, which in turn results in a more frequent incidence of shear bands and, consequently, a more homogeneous distribution of shear. Furthermore, stacking faults may serve as plane barriers to moving dislocations, leading to the domination of slipping in a single slip system and suppression of slipping in all other slip systems, resulting in a shallow neck region.

## References

[1] Fecht H-J, Ivanisenko Yu. Nanostructured materials and composites prepared by solid state processing. In: Koch CC, editor. Nanostructured materials: processing properties, and potential applications. New York: William Andrew Publishing; 2007.

[2] Choi I, Schwaiger R, Kurmanaeva L, Kraft O. Scripta Mater 2009;61:64.

[3] Weertman JR, Farkas D, Hemker K, Kung H, Mayo M, Mitra R, et al. MRS Bull 1999;24:44.

[4] Koch CC, Narayan J. MRS Proc 2000;634:B5.

[5] Kumar KS, Van Swygenhoven H, Suresh S. Acta Mater 2003;51:5743.

[6] Wolf D, Yamakov V, Phillpot SR, Mukherjee A, Gleiter H. Acta Mater 2005;53:1.

[7] Dao M, Lu L, Asaro RJ, De Hosson JTM, Ma E. Acta Mater 2007;55:4041.

[8] Ma E. JOM 2006;58:49.

[9] Zhao YH, Zhu YT, Liao XZ, Horita Z, Langdon TG. Appl Phys Lett 2006;89:121906.

[10] Valiev RZ, Islamgaliev RK, Alexandrov IV. Prog Mater Sci 2000;45:103.

[11] Wang YM, Ma E. Acta Mater 2004;52:1699.

[12] Wang YM, Chen MW, Zhou FH, Ma E. Nature 2002;419:912.

[13] Jia D, Wang YM, Ramesh KT, Ma E, Zhu YT, Valiev RZ. Appl Phys Lett 2001;79:611.

[14] Jia D, Ramesh KT, Ma E. Acta Mater 2003;51:3495.

[15] Cheng S, Ma E, Wang YM, Kecskes LJ, Youssef KM, Koch CC, et al. Acta Mater 2005;53:1521.

[16] Carsley JE, Fisher A, Milligan WW, Aifantis E. Metall Trans A 1998;29:2261.

[17] Carsley JE, Milligan WW, Hackney SA, Aifantis EC. Metall Trans A 1995;26:2479.

[18] Malow TR, Koch CC. Metall Trans A 1998;29:2285.

[19] Jia D, Ramesh KT, Ma E. Scripta Mater 1999;42:73.

[20] Wei Q, Jia D, Ramesh KT, Ma E. Appl Phys Lett 2002;81:1240.

[21] Nieman GW, Weertman Jr JR, Siegel RW. J Mater Res 1991;6:1012.

[22] Wang YM, Wang K, Pan D, Lu K, Hemker KJ, Ma E. Scripta Mater 2003;48:1581.

[23] Sanders PG, Eastman JA, Weertman JR. Acta Mater 1997;45:4019.

[24] Segal VM, Ferrasse S, Alford F. Mater Sci Eng A 2006;422:321.

[25] Crampin S, Vvedensky DD, Monnier R. Phil Mag A 1993;67:1447.

[26] Kestel BJ. Ultramicroscopy 1986;19:205.

[27] Elias H, Hyde DM, Scheaffer RL. A guide to practical stereology. Basel: Karger; 1983.

[28] Dost M, Vogel D, Winkler T, Vogel J, Erb R, Kieselstein E, Michel B. Cross correlation algorithms in digitised video images for object identification, movement evaluation and deformation analysis. In: Doctor Steven R, Bar-Cohen Yoseph, Emin Aktan A, editors. Proceedings of SPIE, vol. 5048. Bellingham, WA: SPIE; 2003.

[29] Binnig G, Quate CF, Gerber C. Phys Rev Lett 1986;56:930.

[30] Elings VB, Gurley JA. US patent no. 5,266,801; 1993.

[31] Tamayo J, Garcia R. Appl Phys Lett 1997;71:2394.

[32] Tamayo J, Garcia R. Appl Phys Lett 1998;73:2926.

[33] Gutkin MY, Gutkin MI, Ovid'ko IA. Plastic deformation in nanocrystalline materials. Amsterdam: Springer; 2004.

[34] Rodriguez P, Krishna Rao K. J Inst Met 1964;65:93.

[35] Humphreys FJ, Hatherly M. Recrystallization and related annealing phenomena. 2nd ed. Oxford: Pergamon Press; 2004.

[36] Rogers HC. Annu Rev Mater Sci 1979;2:283.

[37] Olson GB, Mescall JF, Arzin M. In: Meyers, Murr LE, editors. Shock waves and high strain-rate phenomena in metals. New York: Plenum; 1982.

[38] Sabirov I, Estrin Y, Barnett MR, Timokhina I, Hodgson PD. Scripta Mater 2008;58:163.

[39] Sabirov I, Estrin Y, Barnett MR, Timokhina I, Hodgson PD. Acta Mater 2008;56:2223.

[40] Aernoudt E, Van Houtte P, Leffers T. In: Cahn RW, Haasen P, Kramer EJ, editors. Materials science and technology, vol. 6. Weinheim: VCH; 1993.

[41] Louzguine-Luzgin DV, Vinogradov A, Yavari AR, Li S, Xie G, Inoue A. Phil Mag 2008;88:2979.

[42] Hahn H, Mondal P, Padmanabhan KA. Nanostruct Mater 1997;9:603.

[43] Markmann J, Bunzel P, Rösner H, Liu KW, Padmanabhan KA, Birringer R, et al. Scripta Mater 2003;49:637.

[44] Hasnaoui A, Van Swygenhoven H, Derlet PM. Phys Rev B 2002;66:184112.

[45] Ivanisenko Yu, Kurmanaeva L, Weissmüller J, Yang K, Markmann J, Rösner H, et al. Acta Mater 2009;57:3391.

[46] Valiev RZ, Kaibyshev OA, Sergeev VI, Zelin MS. Res Mech Lett 1984;12:219.

[47] Valiev RZ. Nat Mater 2004;3:511.

[48] Zhao YH, Zhu YT, Liao XZ, Horita Z, Langdon TG. Mater Sci Eng A 2008;463:22.

[49] Wirth BD, Bulatov VV, Diaz de la Rubia T. J Eng Mater Technol 2002;124:329.

[50] Stremel MA. Strength of alloys. Part II: deformation. Moscow: MISIS; 1997 [in Russian].